





Cite this: *Mater. Horiz.*, 2024, 11, 6098

Received 11th July 2024,  
Accepted 11th September 2024

DOI: 10.1039/d4mh00895b

rsc.li/materials-horizons

## A novel approach to chiral separation: thermo-sensitive hydrogel membranes†

Ziyi Huang,<sup>a</sup> Xinjie Shen,<sup>a</sup> Yuxuan Wei,<sup>a</sup> Jia Wei Chew,<sup>c</sup> Edison Huixiang Ang <sup>\*b</sup> and Meilan Pan <sup>\*a</sup>

The application of membrane technology for separating chiral compounds is hindered due to the restricted availability of chiral recognition sites on the membrane surface. In this study, we propose a novel approach for chiral separation through a selector (bovine serum albumin, BSA) mediated thermo-sensitive membrane system. A thermo-sensitive hydrogel-coated membrane (termed PDTAN) was developed by anchoring poly(*N*-isopropylacrylamide) (PNIPAm) onto a polyethersulfone (PES) membrane through an adhesive and hydrophilic dopamine hydrochloride (PDA)/tannic acid (TA)/chitosan (Chi) intermediate layer. The results demonstrate outstanding chiral separation efficiency, achieving  $\alpha_{L/D} = 3.30$  for *D*-phenylalanine (*D*-Phe) rejection at 40 °C on a BSA-mediated PDTAN membrane system, with significant stability and minimal fouling, surpassing previous findings. Moreover, the PDTAN membrane altered the selective properties of recognition sites in BSA, transitioning from rejecting *L*-Phe to rejecting *D*-Phe. Analysis using fourth-order derivative UV-vis, circular dichroism (CD), and *in situ* Fourier transform infrared spectroscopy (FTIR) techniques revealed a transition in the secondary structure of BSA from  $\alpha$ -helix to  $\beta$ -sheet as the temperature increased. This transition, facilitated by hydrogen bonding between BSA and PNIPAm, enabled selective recognition of *D*-Phe, demonstrating a distinct shift in chiral recognition properties. Importantly, with *D*-Phe adsorbed onto  $\beta$ -sheet structures of BSA, hydrogen-bond interactions between BSA and the PDTAN membrane were significantly reduced, thereby minimizing membrane fouling and achieving the durability of membrane-based chiral separation.

### New concepts

A new concept is proposed using thermo-sensitive hydrogel membranes (TSHMs) to construct a selector-mediated membrane system for chiral separation. TSHMs incorporate poly(*N*-isopropylacrylamide) (PNIPAm) onto polyethersulfone (PES) substrates through an innovative intermediate layer made of dopamine hydrochloride (PDA), tannic acid (TA), and chitosan (Chi). Unlike conventional membranes, TSHMs feature a temperature-dependent transition surface that alters the chiral recognition sites of the freedom selector-bovine serum albumin (BSA), causing a structural shift from  $\alpha$ -helix to  $\beta$ -sheet in its secondary conformation. This thermally-induced transition enhances the selectivity of BSA for chiral compounds in separation processes. TSHMs not only expand the responsiveness of modified membrane systems to stimuli beyond pH and ion concentration but also address the limitations of traditional membrane technologies in chiral separation applications.

## Introduction

Ensuring the separation of particular chiral compounds is critical to achieve desirable therapeutic effects and mitigate potential side effects or toxicity.<sup>1–3</sup> Phenylalanine, an aromatic  $\alpha$ -amino acid, exists in two isomeric forms: *D*-phenylalanine (*D*-Phe) and *L*-phenylalanine (*L*-Phe). *L*-Phe is an essential amino acid crucial for protein synthesis and neurotransmitter production, often used in dietary supplements for mood enhancement, while *D*-Phe is studied for its potential analgesic properties. Due to the distinct biological properties and pharmacological activities of *D*-Phe and *L*-Phe, it is crucial to utilize them in their pure forms for specific therapeutic applications.<sup>4</sup> Various methods have been employed to obtain enantiopure species, including column chromatography,<sup>5</sup> crystallization,<sup>6</sup> stereo-selective enzyme catalysis,<sup>7</sup> biosynthesis,<sup>8</sup> and membrane separation.<sup>9</sup> Membrane-based chiral separation has garnered significant attention in research due to its advantages such as high energy efficiency, small footprint, easy preparation, and continuous operability.<sup>10–12</sup> However, despite these benefits, membrane-based chiral separation encounters challenges such as instability, film formation issues, and the need to balance permeability and selectivity.

Enantioselective membranes feature chiral recognition sites designed to selectively bind one of the two enantiomers.<sup>13,14</sup>

<sup>a</sup> College of Environment, Zhejiang University of Technology, Hangzhou, Zhejiang 310014, China. E-mail: mlpan@zjut.edu.cn

<sup>b</sup> Natural Sciences and Science Education, National Institute of Education, Nanyang Technological University Singapore, 637616, Singapore. E-mail: edison.ang@nie.edu.sg

<sup>c</sup> Department of Chemistry and Chemical Engineering, Chalmers University of Technology, 412 96 Gothenburg, Sweden

† Electronic supplementary information (ESI) available. See DOI: <https://doi.org/10.1039/d4mh00895b>

These chiral recognition sites are incorporated into bulk structures such as chiral polymers,<sup>15,16</sup> polysaccharides like chitosan and sodium alginate, and polyamine acid derivatives. Chiral selectors include proteins such as bovine serum albumin (BSA), amino acids, deoxyribonucleic acid (DNA), polypeptides, and crown ether derivatives.<sup>17,18</sup> These recognition sites engage in specific interactions with chiral molecules, including hydrogen bonding, van der Waals forces, and electrostatic interactions.<sup>19</sup> This enables the selective adsorption of one enantiomer while allowing the other to permeate, thus achieving chiral separation.<sup>20–22</sup> Despite these mechanisms, large-scale applications face challenges due to relatively low binding capacities and limited preferential binding affinities, which impede the membrane's permeability and selectivity.<sup>23,24</sup>

Poly(*N*-isopropylacrylamide) (PNIPAm) is a thermosensitive polymer that has garnered significant attention due to its lower critical solution temperature (LCST) of approximately 32 °C.<sup>25,26</sup> This polymer features hydrophilic amino and hydrophobic isopropyl groups along its macromolecular chain, enabling rapid swelling and contraction of the PNIPAm hydrogel through a hydrophilic–hydrophobic transition at the LCST.<sup>27–29</sup> When integrated into a membrane matrix, the hydrophobicity of PNIPAm can be manipulated to control effective pore size and transmembrane permeability. Upon heating above the LCST, dehydration occurs around the hydrophobic isopropyl groups, triggering a structural change in the polymer backbone.<sup>30,31</sup> This transition alters the environment surrounding the chiral recognition sites, thus allowing for the adjustment of the selectivity and binding affinity of these sites. Although the promising potential of temperature-responsive control for enhancing membrane-based chiral separation remains underexplored, it provides the impetus for the current study.

In this work, hydrogel-like membranes (denoted as PDTAN) were successfully fabricated by anchoring poly(*N*-isopropylacrylamide) (PNIPAm) onto polyethersulfone (PES) membranes using an adhesive and hydrophilic intermediate layer composed of dopamine hydrochloride (PDA), tannic acid (TA), and chitosan (Chi). The chemical properties, biocompatibility, and temperature-responsive characteristics of these thermosensitive membranes were investigated. The chiral separation performance for D,L-Phe was systematically examined. The study focused on the integration of PNIPAm within chiral membranes and assessed the impact of temperature-induced structural changes on chiral separation efficiency. Combining experimental characterization and theoretical modeling, the mechanisms underlying thermo-sensitive chiral separation were elucidated, and the feasibility for large-scale applications was evaluated. The findings suggest that thermo-sensitive chiral membranes offer enhanced selectivity and permeability, potentially overcoming existing limitations in conventional chiral separation techniques. By providing insights into the temperature-dependent chiral separation process, this research paves the way for the development of advanced membrane-based technologies for enantioseparation in various industrial applications.

## Experimental

### Reagents and materials

D,L-Phenylalanine (D,L-Phe, 99%) and dopamine hydrochloride (PDA, 99%), tannic acid (TA, 99%), tris(hydroxymethyl) amino-methane hydrochloride (Tris-HCl, 99%), and sodium hydroxide (NaOH, 99.0%) were purchased from Shanghai Damas-beta Co., Ltd. Chitosan (Chi, degree of deacetylation > 95.0%), ammonium formate (>99.0% HPLC), formic acid (>99.0%, HPLC), and poly(*N*-isopropylacrylamide) (PNIPAm) were obtained from Shanghai Macklin. Biochemical Co., Ltd provided the bovine serum albumin (BSA), while Shanghai Yuan Ye Bio-Technology Co., Ltd supplied the polyethersulfone membrane (PES) with a 50 kDa molecular weight cutoff (MWCO) from RisingSun Membrane Technology (Beijing) Co., Ltd. Unless otherwise indicated, all chemicals were purchased from commercial sources in analytically pure form and used as-is.

### Preparation of modified membranes

The synthesis of the various modified PES membranes begins with soaking the PES membrane in deionized water for 40 min to remove the protective layer, followed by drying for subsequent use. For the PDTA membrane, 150 mL of 0.5 mM Tris buffer is prepared, and the pH is adjusted to 8.5 using 0.1 mol L<sup>−1</sup> NaOH. Subsequently, 0.2 g of PDA and 0.8 g of TA are added and mixed thoroughly using ultrasound. The membrane is then immersed in the solution, rinsed to remove unreacted materials, and dried in an oven at 50 °C. For the PDTN membrane, a similar initial process is followed, but after preparing the Tris buffer and adding PDA and TA, 0.1 g of PNIPAm is also added. The membrane is placed in the Tris solution and stirred on a shaking table at 45 °C and 120 rpm for 1 h, followed by rinsing and oven drying at 50 °C. In the synthesis of the PDCN membrane, the Tris buffer is prepared, and the pH is adjusted as before, with 0.2 g of PDA added and mixed using ultrasound. The membrane is immersed in this solution with an additional 0.1 g of chitosan and 0.1 g of PNIPAm, then stirred on a shaking table at 45 °C and 120 rpm for 1 h, before rinsing and drying in an oven at 50 °C. For the PDTAN membrane fabrication, after soaking and drying the PES membrane, 150 mL of 0.5 mM Tris buffer is prepared, and the pH is adjusted to 8.5 with 0.1 mol L<sup>−1</sup> NaOH. Then, 0.2 g of PDA and 0.8 g of TA are added and mixed using ultrasound. The membrane is placed in this solution with 0.1 g of chitosan and 0.1 g of PNIPAm, stirred on a shaking table at 45 °C and 120 rpm for 1 h, followed by rinsing and drying in an oven at 50 °C. The detailed steps for the fabrication of PDTAN are illustrated in Fig. S1 (ESI<sup>†</sup>).

### Membrane characterization

The freeze-dried samples were quenched by freeze-drying, and their surfaces and sections were gold-sprayed in a vacuum environment. The surface and section morphologies of different membranes were characterized using scanning electron microscopy (SEM; JEOL JEM-IT800). The chemical compositions of the membranes were verified by X-ray diffraction pattern (XRD; Rigaku Ultima IV, Japan) and X-ray photoelectron spectroscopy

(XPS; Thermo Scientific K-Alpha, America). Contact angles at different temperatures on the surfaces of various modified membranes were measured using a contact angle goniometer (JC2000C, China). Fourier transform infrared spectroscopy (FTIR; Thermo Scientific Nicolet iS20) was employed to analyze the total reflection spectra of membrane surfaces to identify changes in surface functional groups with temperature. The wave number range of the test was 600–4000  $\text{cm}^{-1}$ . Protein concentrations were determined using a UV spectrophotometer (T6, PWESEE, China), and D,L-Phe concentrations were determined by high performance liquid chromatography (HPLC; 1260 Infinity II, Agilent).

### Ultrafiltration experimental setup and method

All experiments were carried out using a crossflow cell (CF042A, Sterlitech corporation, USA) with an effective membrane area of 42.3  $\text{cm}^2$  (9.2  $\text{cm} \times 4.6 \text{ cm}$ ), and a hold-up volume of 17 mL. The schematic of the ultrafiltration setup is shown in Fig. S2 (ESI†). Specifically, the feed side of the cell was connected to the feed tank (2 L), whose temperature was controlled by a chiller (THD-0506, Shimadzu electronic, China) at  $20\text{--}50 \pm 0.5^\circ\text{C}$ . The feed was pumped (BT100-2J + 2\*YZ1515, Rongbai pump, China) at a rate of 100  $\text{mL min}^{-1}$  (measured by a flowmeter LZB-3WB6, Dahua corporation, China), which was controlled by a variable speed drive (Q91SA-PN6, Dahua corporation, China). A back-pressure regulator was employed to set the transmembrane pressure (TMP) to 50 kPa. The permeate was collected in the permeate tank and the mass increase was continuously monitored using a digital balance (YP20002B, Lichen corporation, China) to quantify permeate flux. Permeate was recycled back to the feed tank every 5 minutes to maintain an approximately constant feed concentration.

BSA and D,L-Phe were dissolved in water to obtain feed concentrations of 0.1 mM and 0.5 mM, respectively. The obtained solutions were stirred at 400 rpm (SN-MS-3D, SUNNE, China) with a magnetic stirring bar for 2 h before use. A new membrane was used each time. Prior to filtration, each membrane was flushed with water to remove any contaminants, and then filtered with water for 2 h to obtain a stable initial flux ( $J_0$ ,  $\text{L m}^{-2} \text{ h}^{-1} \text{ bar}^{-1}$ ) before introducing the targeted feed.

$$J_0 = \frac{V}{A \times t \times P} \quad (1)$$

where  $V$  represents the permeate volume collected during the sampling interval  $t$ ,  $A$  represents the effective area of the membrane,  $t$  represents the measurement time, and  $P$  represents the transmembrane pressure.

During the 2 h of ultrafiltration, 1 mL of feed and 2 mL permeate were collected every 10 min for analyses. The feed was diluted 10 times for UV-vis analysis and the permeate was analysed using HPLC.

### Characterization of chiral separation performance

The concentrations of BSA in the feed and permeate were determined by a UV-vis spectrometer at the wavelength of

277.0 nm. BSA rejection was calculated by:<sup>32</sup>

$$R_{\text{BSA}} = 1 - \frac{C_{\text{P,BSA}}}{C_{\text{f,BSA}}} \quad (2)$$

where  $R_{\text{BSA}}$  stands for the retention rate,  $C_{\text{P,BSA}}$  stands for the concentration of BSA in the permeate solution, and  $C_{\text{f,BSA}}$  stands for the concentration of BSA in the feed solution. While the 50 kDa PES membrane was expected to completely retain the 66.4 kDa BSA, the retention rate of BSA was approximately 98%, which is likely due to the range of membrane pore sizes (Fig. S3, ESI†).

The D-Phe and L-Phe concentrations in the feed and permeate were determined by HPLC at the wavelength of 220.0 nm with an InfinityLab Poroshell chiral-T column (Agilent). The mobile phase was 30 mL of methanol and 70 mL of 50 mM ammonium formate (pH = 3.6) at a flow rate of 0.5  $\text{mL min}^{-1}$  at  $25^\circ\text{C}$ .

The separation factor,  $\alpha$ , was used to characterize the chiral separation performance:<sup>33</sup>

$$\alpha = \frac{\frac{C_{\text{P,L-Phe}}}{C_{\text{P,D-Phe}}}}{\frac{C_{\text{f,L-Phe}}}{C_{\text{f,D-Phe}}}} \quad (3)$$

where  $C$  is the concentration, while the subscript  $P$  stands for permeate and  $f$  for feed. The peak area in HPLC was used to quantify concentration.

The water permeance ( $J_w$ ,  $\text{L m}^{-2} \text{ h}^{-1} \text{ bar}^{-1}$ ) was calculated by:

$$J_w = \frac{\Delta V}{A \times \Delta t \times \Delta P} \quad (4)$$

where  $\Delta V$  represents the permeate volume collected,  $A$  represents the effective area of the membrane,  $\Delta t$  represents the measurement time, and  $\Delta P$  represents the transmembrane pressure.

## Results and discussion

### Preparation and characterizations of modified membranes

BSA, the chiral selector with a molecular weight of approximately 66.4 kDa, exceeds the molecular weight cutoff of 50 kDa. BSA preferentially binds with L-phenylalanine (L-Phe) to form a larger complex retained by the membrane, while free D-phenylalanine (D-Phe) permeates through,<sup>34</sup> facilitating the separation of the D,L-Phe mixture (Fig. 1a). The interaction between BSA and L-Phe is significantly influenced by the chemical properties of the membrane surface.<sup>35</sup> Specifically, stronger binding interactions between D,L-Phe and the pristine membrane surface compared to those between L-Phe and BSA impede the separation process. To mitigate this, the pristine membrane surface can be modified to reduce its binding affinity for D,L-Phe. The schematic diagram of the cross-linking reaction of the hydrogel-like materials (PDTCN) on PES membranes is shown in Fig. 1b. For the fabrication of the PDTCN membrane, an adhesive and hydrophilic PDA/TA intermediate layer was first introduced to obtain the PDTA

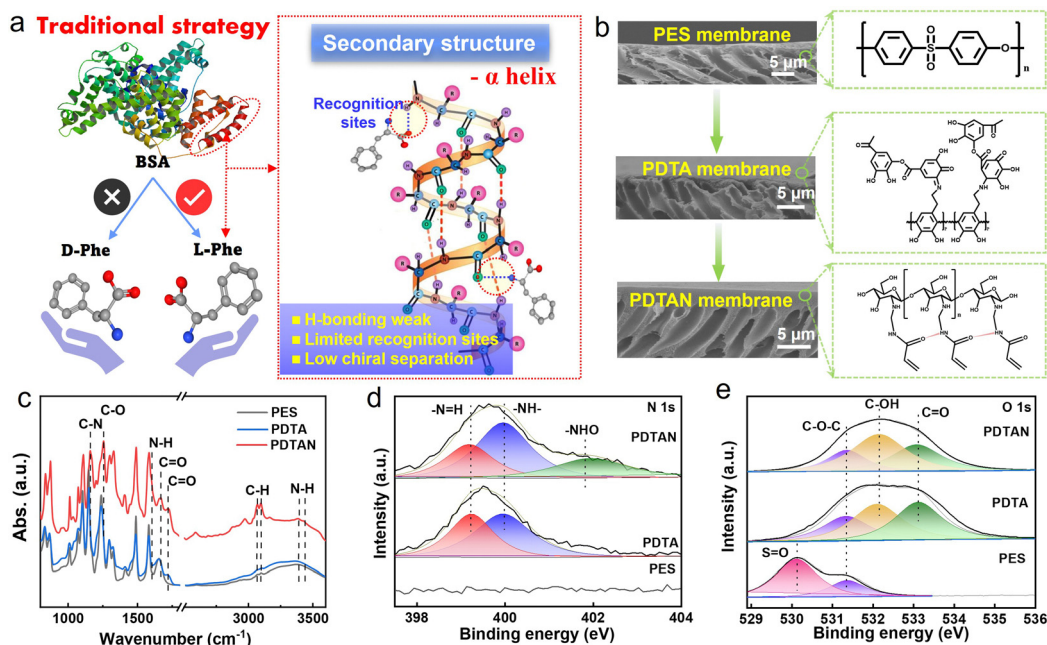


**Fig. 1** (a) Schematic illustration of the process of chiral separation in hydrogel-coated membranes. (b) SEM images and molecular structures of PES, PDTA and PDTAN membranes. Characterization of PES and PDTAN membranes: (c) FTIR spectra, (d) N 1s and (e) O 1s of XPS analysis of PES, PDTA and PDTAN.

membrane. After PDA/TA deposition, the micropores on the membrane surface were covered by a cross-linked PDA/TA network based on the Michael addition and/or Schiff base reactions.<sup>36,37</sup> Furthermore, the PNIPAm was anchored onto the PDTA membrane through chitosan (Chi), yielding the PDTAN membrane. The surface of the PDTAN membrane had a much more rough and compact morphology than PDTA and PES membranes. A significant color change was observed post-modification, as illustrated in Fig. S4 (ESI†). Furthermore, the formation of a distinct surface layer was evident, and the pore size was found to be larger than that of the pristine PES membrane. The abundant hydrophilic –OH groups within the polymer matrix enhanced water/polymer hydrogen bonding while weakening water/water interactions.<sup>38</sup> This effect is evident in the hydrophilic Chi/PNIPAm layer, which increased the hydrophilicity of the PDTAN membrane, resulting in a decrease in the contact angle (CA) from 69° to 48° (Fig. S5, ESI†).

ATR-FTIR spectroscopy was employed to confirm the chemical composition of the PDTAN membrane (Fig. 1c and Fig. S6, ESI†). In the PES membrane, the distinctive peak at 1035.2 cm<sup>−1</sup> is attributed to the stretching vibrations of the S=O bond.<sup>39</sup> Following PNIPAm modification, a noticeable peak at 3163.5 cm<sup>−1</sup>, corresponding to the surface N–H stretching mode,<sup>40</sup> indicates the successful incorporation of PNIPAm. Additional characteristic peaks at 1667.3 cm<sup>−1</sup> (C=O stretching, amide I) and 1596.0 cm<sup>−1</sup> (N–H bending, amide II) further confirm the presence of PNIPAm.<sup>41,42</sup> The copolymerization process was validated by the emergence of new peaks at 1717.3 cm<sup>−1</sup> (C=O stretching) and 1253.7 cm<sup>−1</sup> (C–O stretching), which are associated with the integration of monomers into the polymer matrix. XPS analysis of N 1s and O 1s was

conducted to investigate the surface elemental composition of the membranes (Fig. S7, ESI†). The increased N–H peak at 400.0 eV further confirmed the successful integration of PNIPAm on the membrane surface (Fig. 1d). The presence of a peak at 401.4 eV in the N 1s analysis, corresponding to –NHO, indicates effective hydrogen bond formation between –NH and –C=O, substantiating the construction of the thermally responsive network in PDTAN. Moreover, the absence of the S=O peak at 530.2 eV suggests uniform hydrogel incorporation on the PES membrane. The presence of C–OH (532.2 eV) and C=O (533.2 eV) bonds in the hydrogel-coated membrane indicates that cross-linking reactions have occurred (Fig. 1e).

### Chiral separation performance

In order to examine the chiral separation efficiency of the modified membranes, chiral separation experiments were performed using a cross-flow cell (Fig. S2, ESI†). The mixture of D,L-Phe (ratio of 1 : 1) and BSA was used as the feed. Fig. 2a illustrates the exceptional performance of the PDTAN membrane, achieving an  $\alpha_{L/D}$  value of 3.3 (Fig. 2b). In contrast, the unmodified PES membrane has an  $\alpha_{L/D}$  value of 0.74, indicating no significant separation capability. The presence of the PNIPAm layer is crucial for the membrane's ability to separate D-Phe and L-Phe, as shown by the reduced chiral performance of PDTA ( $\alpha_{L/D}$  = 1.7) without the PNIPAm layer. Additionally, the marked decrease in chiral separation efficiency in PDTN ( $\alpha_{L/D}$  = 0.9) and PDCN ( $\alpha_{L/D}$  = 1.1) membranes, which lack the intermediate Chi and TA layer, underscores the vital role of this adhesive and hydrophilic intermediate layer. BSA acted as the chiral selector, providing the primary chiral recognition sites that preferentially bind with D-Phe or L-Phe to form larger complexes retained by the membrane.



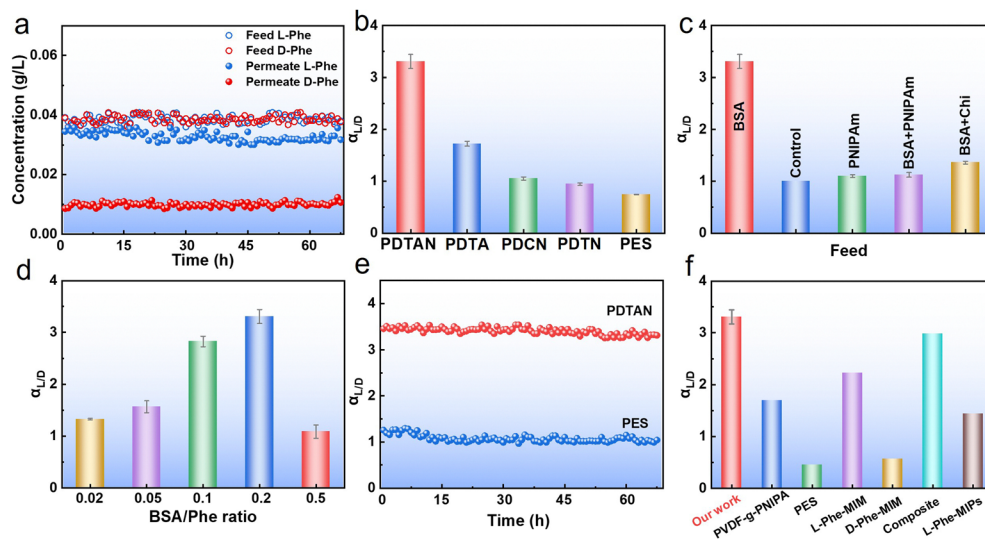


**Fig. 2** (a) D,L-Phe concentration of PDTAN membrane in feed and permeate at 40 °C. (b) Chiral separation efficiency of the different membranes at a feed temperature of 40 °C and absolute pressure of 50 kPa. The effects of various parameters on the chiral separation efficiency of PDTAN membranes: (c) feed type, and (d) Phe/BSA ratio. (e) Chiral separation performance of PES and PDTAN membranes over more than 60 h. (f) Chiral separation efficiency comparison of PDTAN membranes with commercial and reported membranes (detailed conditions are listed in Table S1, ESI†).

The hydrogel-coated membrane is crucial for mitigating interfacial interactions with the membrane, thus enabling chiral separation. Given the positive effects of PNIPAm and Chi on chiral separation, the roles of these components as chiral selectors were evaluated. Fig. 2c demonstrates that PNIPAm and Chi do not serve as chiral selectors; instead, their presence inhibited the chiral activity of BSA. With the Phe concentration held constant at 0.5 mM, varying BSA concentrations yielded ratios of BSA to Phe concentrations spanning from 0.02 to 0.5. Fig. 2d demonstrates peak separation efficiency at a ratio of 0.2 ( $\alpha_{L/D} = 3.30$ ).

However, elevated BSA concentrations above this optimal ratio hindered chiral separation by promoting aggregation through thiol-disulfide interchange, thereby reducing the accessibility of the  $\alpha$ -helix involved in binding with L-Phe.<sup>43,44</sup> While increasing

pressure leads to higher flux (Fig. S8, ESI†), it has been reported to affect chiral separation efficiency negatively.<sup>45</sup> Fig. S9 (ESI†) illustrates approximately similar chiral separation efficiencies for pressures of 10–60 kPa, suggesting the structural stability of the modified membranes in this pressure range. Additionally, comparing the PDTAN membrane with other reported membranes, Fig. 2f shows that the PDTAN membrane offered better chiral separation of D,L-Phe.

### Role of PNIPAm as a thermo-sensitive polymer in chiral separation

PNIPAm is a temperature-responsive polymer with a lower critical solution temperature (LCST) around 32 °C,<sup>46</sup> at which it undergoes reversible swelling/contraction phase transitions,

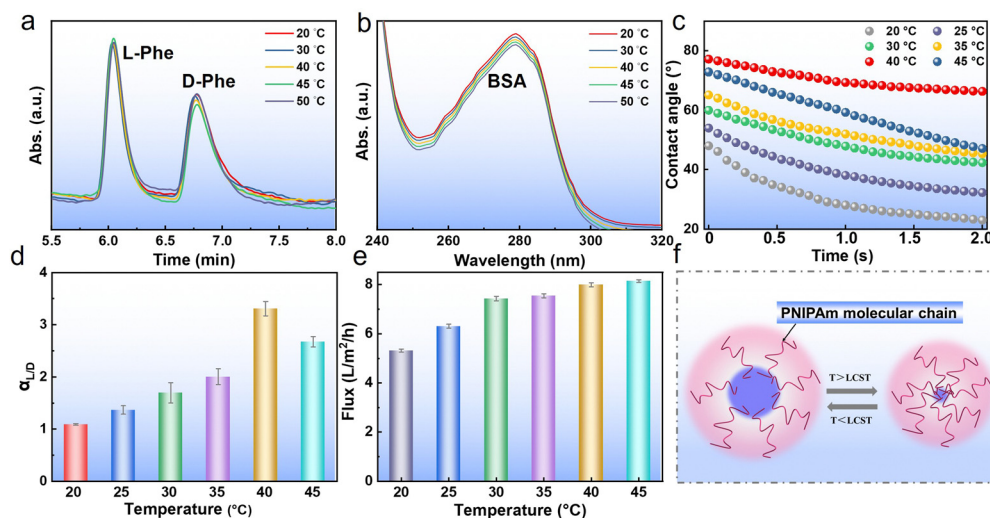


**Fig. 3** Effect of temperature on the PDTAN membrane: (a) HPLC results, (b) UV-vis spectra, (c) contact angles, (d) chiral separation efficiency, and (e) flux vs. time. (f) Schematic illustration of thermoresponsive properties of the PNIPAm molecular chain.

offering the capability to modulate BSA adsorption through temperature adjustments.<sup>47</sup> However, it has been noted that the solubility, thermal stability, and diffusion rates of Phe/BSA, as well as membrane selectivity, vary with feed temperature.<sup>48</sup> To mitigate the impact of BSA or Phe conformational changes at higher temperatures, the influence of temperatures ranging from 20–50 °C was evaluated. Fig. 3a and Fig. 3b indicate minimal changes in the intensities of characteristic peaks of Phe in HPLC and BSA in UV-vis, suggesting the chemical stability of Phe and BSA within this temperature range. Characterizing contact angles proves instrumental in discerning the thermally sensitive properties of surfaces or materials. The assessment of contact angle serves as a valuable tool for elucidating the thermosensitive properties exhibited by surfaces or materials.<sup>49</sup> Fig. 3c presents the evolution of water contact angles over 2 seconds at different temperatures. Initially, the contact angles decrease sharply before reaching a plateau at each temperature. Furthermore, contact angles increase with temperature, reaching 77.2° at 40 °C, indicating increased hydrophobicity of the PDTAN membrane surface. Below 40 °C, the PDTAN membrane exhibits higher hydrophilicity, transitioning towards hydrophobicity above 40 °C, resulting in phase separation from the aqueous medium. These observations highlight the role of thermally-responsive PNIPAM chains in governing the membrane selectivity of PDTAN membranes. Fig. 3d illustrates the temperature-dependent sensitivity of the chiral separation efficiency of the PDTAN membrane, notably achieving a peak separation factor  $\alpha_{L/D}$  of 3.30 at 40 °C, with a subsequent decline in  $\alpha_{L/D}$  observed beyond this temperature. Fig. 3e demonstrates the temperature sensitivity of flux, highlighting increased diffusion rates. Membranes that exhibit higher selectivity for chiral compounds often show improved chiral separation efficiency; however, this is typically accompanied by a trade-off with permeate flux, as membranes with greater selectivity tend to have reduced flux.<sup>50</sup> Hence, it can be deduced that

membrane selectivity is notably affected by the feed temperature. PNIPAM within the PDTAN membrane is recognized as a temperature-responsive polymer capable of undergoing reversible phase transitions in response to temperature variations (Fig. 3f).<sup>51</sup>

### Antifouling performance

BSA is well-known for its fouling propensity, which can impair chiral separation performance.<sup>52</sup> The pristine PES membrane exhibited significant fouling, as evident from the noticeable color change in Fig. 4a, compromising its ability for chiral separation. In contrast, the PDTAN membrane appeared similar after filtration, indicating its superior fouling resistance. The pristine PES membrane exhibited a high susceptibility to BSA fouling, as evidenced by its initial permeate flux of 20.02 L m<sup>-2</sup> h<sup>-1</sup> bar<sup>-1</sup>, which rapidly declined to 7.93 m<sup>-2</sup> h<sup>-1</sup> bar<sup>-1</sup> (Fig. 4c), reflecting a significant 60.4% decline over 65 h (Fig. 4d). In contrast, the PDTAN membrane sustained a stable permeate flux of 10.34 L m<sup>-2</sup> h<sup>-1</sup> bar<sup>-1</sup> and demonstrated near-perfect D-Phe rejection over 80 h (Fig. 4d), indicating its superior fouling resistance. After the fouling test, the PDTAN membrane remained clean, without BSA-foulant, unlike the BSA-adsorbed PES membrane. In comparison, the permeate flux of PDTA (68.41%), PDTN (59.63%), and PDCN (35.33%) membranes decreased markedly, which correlates with their chiral separation efficiency results (Fig. S10, ESI†). Compared to reported chiral separation techniques (Table S1, ESI†), the developed PDTAN membrane *via* a facile and environment-friendly strategy, showcased durable and comparable chiral separation performance, particularly in its resistance to fouling.

### Chiral recognition transitions in thermosensitive networks

As previously mentioned, the recognition site on BSA plays a pivotal role in the selective chiral separation of D-Phe and L-Phe. To delve deeper into the chiral recognition mechanism of BSA,

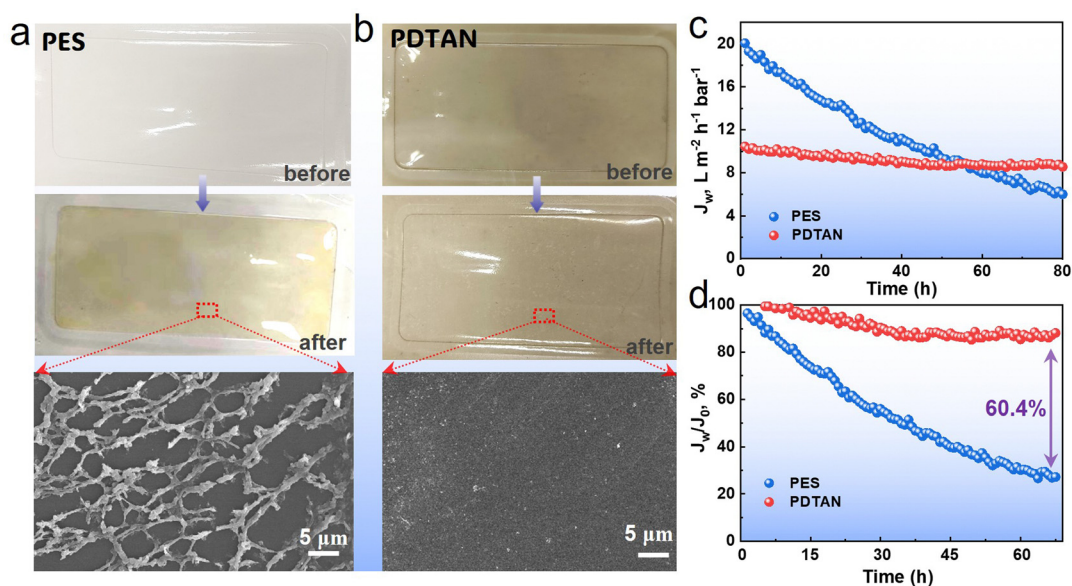


Fig. 4 Photographs and SEM images of PES (a) and PDTAN (c) membranes before and after separation.  $J_w$  (c) and  $J_w/J_0$  (e) of PES and PDTAN membranes. The feeds were 0.1 mM BSA and 0.5 mM D,L-Phe, with a constant temperature of 40 °C and a pressure of 50 kPa.

UV-vis and circular dichroism (CD) analysis were employed to elucidate the changes in its secondary structure. Fig. 5a illustrates the correlation between BSA and Phe/PNIPAm as depicted by the fourth derivative derived from UV-vis spectra (Fig. S11, ESI†).<sup>53</sup> The fourth-order derivative of the BSA UV spectrum exhibits seven distinct absorption peaks. Specifically, the peaks centred around 253, 258, 264, and 268 nm correspond to the characteristic peaks associated with Phe residues, while the peak at 278 nm represents the characteristic peak of the Tyr residue. Additionally, the peak at 284 nm is an overlapping characteristic peak of Tyr/Trp, and the peak at 290.5 nm corresponds to the characteristic peak of the Trp residue. Upon the addition of D,L-Phe or PNIPAm, the changes in the wavelengths of characteristic absorption peaks of different types of aromatic amino acid residues were observed, indicating alterations in their respective microenvironments.

CD spectroscopy is a robust and highly sensitive technique employed for discerning the conformational intricacies of proteins.<sup>54</sup> In this study, far-UV and CD were employed to investigate the secondary structural alterations of BSA induced by the presence of D/L-Phe and PNIPAm (Fig. 5b). Notably, the CD spectra of BSA exhibit prominent bands at 208 and 222 nm, which are the characteristic peaks indicative of the  $\alpha$ -helical structure.<sup>55</sup> These signals arise from the peptide's  $n-\pi^*$  and  $\pi-\pi^*$  transitions. The precise position of these peaks is contingent upon the transition energies between the ground and electronic excited states of polarizable electrons within the protein. It is generally observed that the permanent or induced dipoles of solvent molecules interact with the electrons within the peptides, thereby potentially stabilizing or destabilizing the energy levels of these electronic states. Consequently, alterations in the solvent environment led to perturbations in transition energy, thereby resulting in shifts in the absorption band peaks of the peptides.

The analysis of Fig. 5c reveals a significant alteration in the shape and positioning of the peaks in the presence of D,L-Phe, implying a modification in the secondary structures of BSA following its interaction with D,L-Phe. The transition from

$\alpha$ -helix to  $\beta$ -sheet conformation is prominently observed. Increasing concentrations of D,L-Phe show a gradual decrease in  $\alpha$ -helix structures (Fig. S12, ESI†), indicative of effective binding to essential BSA polypeptide residues crucial for chiral separation. Notably, PNIPAm also interacts with BSA, leading to a similar decline in  $\alpha$ -helix structures (Fig. S13, ESI†). The combined influence of D,L-Phe and PNIPAm results in an obvious transformation of  $\alpha$ -helix structures into  $\beta$ -sheet formations (Fig. 5d), likely mediated by alterations in hydrogen bonding interactions (Fig. 5e). Therefore, PNIPAm provides additional hydrogen bonding sites that facilitate greater adsorption of BSA, resulting in the formation of  $\beta$ -sheet structures. The proportion of  $\beta$ -sheet structures is higher in the presence of Phe and PNIPAm compared to either Phe or PNIPAm alone. This suggests that PNIPAm facilitates the formation of  $\beta$ -sheet structures on BSA and can provide more effective recognition sites for Phe, which is adsorbed onto BSA and subsequently rejected, supporting the results of chiral separation performance. This may facilitate minimization of membrane fouling and ultimately achieve greater durability in membrane-based chiral separation.

### Chirality transitions in thermosensitive networks

According to the above analysis, the  $-\text{NH}_2$  groups present in Chi segments play a crucial role in forming physically cross-linked networks within PNIPAm. These  $-\text{NH}_2$  groups not only facilitate the construction of crosslinked networks through hydrogen bonding and ionic interactions, but also significantly influence the thermal responsiveness of the PNIPAm networks, resulting in alterations in swelling and deswelling dynamics. It is observed that the crosslinked nanogel network, resembling a hydrogel, undergoes continuous shrinkage beyond LCST. For the fabrication of a thermo-responsive membrane, a monomer with strong water absorbing properties ( $-\text{OH}$ ) and a phenyl group with large steric hindrance are copolymerized with PNIPAm and Chi to form a terpolymer (PDTAN) (Fig. 6a). The resulting PDTAN membrane exhibited exceptional efficiency in chiral separation at the LCST (40 °C). Remarkably, the introduction of a PNIPAm active layer to undergo a temperature-triggered sol-gel transition retained good structural stability even at temperatures above the LCST (Fig. 6b). As the temperature increased, there was a continuous transformation of secondary structures within BSA, transitioning from  $\alpha$ -helix to  $\beta$ -sheet, with the proportion of the  $\beta$ -sheet structure per 100 residues increasing from 4.20 (20 °C) to 5.39 (40 °C) (Fig. S13, ESI†). This transformation can be attributed to the presence of  $-\text{C}=\text{O}$  and  $-\text{N}-\text{H}$  groups in PNIPAm, which effectively maintains the  $\beta$ -sheet structure of BSA, thereby preventing its return to the original  $\alpha$ -helix structure. Notably, the  $\beta$ -sheet structure of BSA demonstrates efficient recognition of D-Phe molecules, facilitating their binding and selective rejection (Fig. 6c). The recognition properties of the  $\beta$ -sheet structures are distinctly different from those of  $\alpha$ -helix structures, leading to a transformation in chiral recognition capacities. Additionally, the interaction between  $\beta$ -sheet structures and the PNIPAm membrane is minimal, thereby inhibiting the formation of

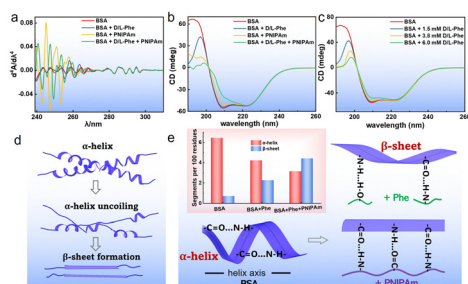


**Fig. 5** Fourth derivative of UV-vis (a) and CD (b) spectra of the BSA structure under different conditions. (c) CD spectra of BSA with different concentrations of D,L-Phe. (d) Schematic of the keratin protein secondary structure rearrangement from  $\alpha$ -helix to  $\beta$  sheet. (e) Schematic showing the hydrogen bond network that is responsible for the formation of the keratin secondary structures. The inset figure is the change in the bond orientation within the Phe and PNIPAm as keratin rearranges from the  $\alpha$  structure to the  $\beta$  structure, as depicted in Fig. 5b.



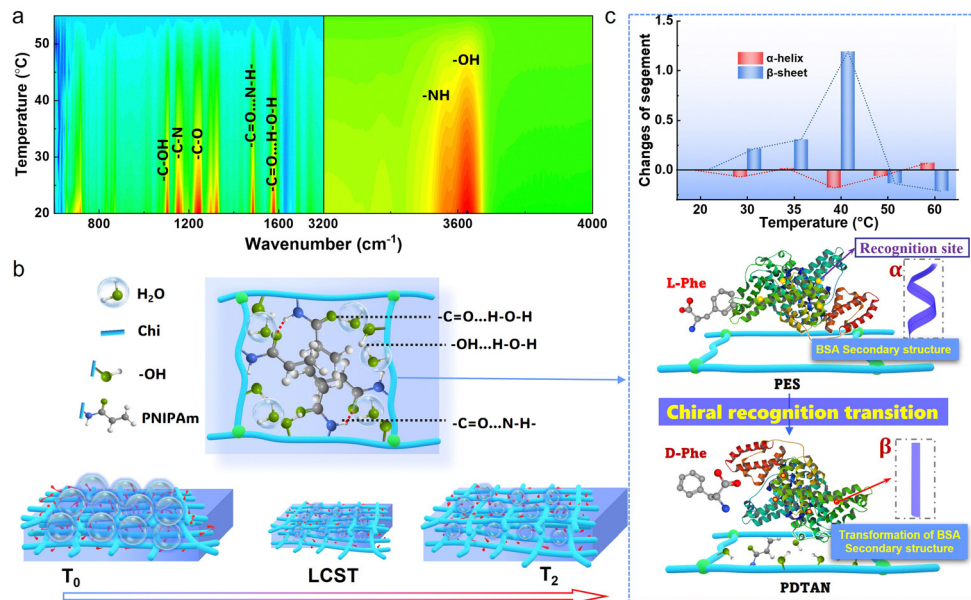


Fig. 6 (a) Temperature-dependent FTIR spectrum of the PDTAN membrane during heating from 20 °C to 50 °C. (b) Schematic illustration of the thermo-sensitive properties of the PDTAN membrane. (c) Changes of  $\alpha$ -helix and  $\beta$  sheet segments at different temperatures via analysis of the CD spectra in Fig. S14 (ESI<sup>†</sup>); schematic illustrating the mechanism of the chirality transition of BSA coupling with thermosensitive networks.

foulants on the membrane surface and consequently enhancing the chiral separation capacity. However, as the temperature approaches and exceeds the LCST, the polymer chains undergo a collapse, leading to a reduction in the membrane's overall swelling capacity. This collapse results in a diminished effective surface area available for interactions with chiral molecules, ultimately contributing to a decline in chiral separation performance.

## Conclusions

In conclusion, we synthesized a thermally responsive PDTAN hydrogel-coated membrane by anchoring PNIPAm onto a PES membrane through a PDA/TA/Chi intermediate layer. The resulting membrane exhibited outstanding efficiency in chiral separation, achieving a peak  $\alpha_{L/D}$  value of 3.30 for rejecting D-Phe at 40 °C. Importantly, this modification shifted the specificity of the membrane from rejecting L-Phe to rejecting D-Phe. Through fourth-order derivative UV-vis spectroscopy, circular dichroism (CD), and *in situ* FTIR analysis, we observed a temperature-induced transition in BSA secondary structure from  $\alpha$ -helix to  $\beta$ -sheet. Hydrogen bonding interactions between BSA and PNIPAm stabilized the  $\beta$ -sheet structure, facilitating selective recognition of D-Phe. Additionally, adsorption of D-Phe onto the  $\beta$ -sheet structures of BSA, reduced membrane fouling, thereby enhancing chiral separation efficiency. This study represents a significant advancement in chiral membrane separation by exploiting structural transitions in chiral selectors to improve selective recognition capabilities.

## Author contributions

Ziyi Huang: conceptualization, methodology, data curation, writing – original draft, writing – review & editing, and

visualization. Xinjie Shen: investigation. Yuxuan Wei: investigation. Jia Wei Chew: supervision. Meilan Pan: conceptualization, project administration, funding acquisition, and writing – review & editing. Edison Huixiang Ang: project administration, funding acquisition, and writing – review & editing.

## Data availability

Data will be made available on request.

## Conflicts of interest

The authors declare no competing interests.

## Acknowledgements

We gratefully acknowledge the financial support from the National Natural Science Foundation of China (Grant No. 22106139), and Basic Scientific Research Projects in Colleges and Universities funded by Zhejiang Province (RF-A2022009) and Ministry of Education, Singapore, under its Academic Research Fund Tier 1 (RG88/23 and RG10/22).

## Notes and references

- 1 R. Hinchet, U. Khan, C. Falconi and S.-W. Kim, *Mater. Today*, 2018, **21**, 611–630.
- 2 S. A. Han, T. H. Kim, S. K. Kim, K. H. Lee, H. J. Park, J. H. Lee and S. W. Kim, *Adv. Mater.*, 2018, **30**, 1800342.
- 3 H. L. Qian, S. T. Xu and X. P. Yan, *Anal. Chem.*, 2023, **95**, 304–318.



- 4 H. Khan, T. Khan and J. K. Park, *Sep. Purif. Technol.*, 2008, **62**, 363–369.
- 5 E. Lesellier and C. West, *J. Chromatogr. A*, 2015, **1382**, 2–46.
- 6 H.-S. Choi, I. H. Oh, B. Zhang, G. Coquerel, W. S. Kim and B. J. Park, *J. Phys. Chem. C*, 2024, **15**, 4367–4374.
- 7 G. Liu, L. Wang, F. Zhu, Q. Liu, Y. Feng, X. Zhao, M. Chen and X. Chen, *Chem. Eng. J.*, 2022, **428**, 131975.
- 8 V. K. Vashistha, R. Bala, A. Mittal and R. V. S. R. Pullabhotla, *Sep. Sci. Technol.*, 2023, **58**, 2138–2144.
- 9 Y. Xiao and T. Chung, *J. Membr. Sci.*, 2007, **290**, 78–85.
- 10 T. Liu, Z. Li, J. Wang, J. Chen, M. Guan and H. Qiu, *Chem. Eng. J.*, 2021, **410**, 128247.
- 11 W. Chen, X. Qiu, Y. Chen, X. Bai, H. Liu, J. Ke, Y. Ji and J. Chen, *Sep. Purif. Technol.*, 2023, **327**, 124898.
- 12 C. Yu, B. H. Yin, Y. Wang, S. Luo and X. Wang, *Coord. Chem. Rev.*, 2023, **495**, 215392.
- 13 M. Gogoi, R. Goswami, A. Borah, C. Bhuyan, H. Sarmah and S. Hazarika, *J. Chem. Sci.*, 2022, **134**, 89–107.
- 14 S. Nono-Tagne, Y. Navon, Y. Ogawa, B. Carré and I. Otsuka, *Cellulose*, 2023, **31**, 2765–2782.
- 15 J. Wang, T. Wu, D. Li, Z. Shi, J. Liu, Y. Zang and T. Aoki, *Sep. Purif. Technol.*, 2024, **340**, 126833.
- 16 M. Milovanovic, F. Tabakoglu, F. Saki, E. Pohlkoetter, D. Buga, V. Brandt and J. C. Tiller, *J. Membr. Sci.*, 2023, **668**, 121190.
- 17 C. Tortolini, V. Gigli, F. Rizzo, A. Lenzi, M. Bizzarri, A. Angeloni and R. Antiochia, *Sensors*, 2023, **23**, 23229211.
- 18 J. Wang, S. Han, H. Zhao, H. Li, X. Niu, Y. Wang and K. Wang, *Electroanalysis*, 2023, **36**, 202300301.
- 19 M. Zheng, Z. Jin, Z. Ma, Z. Gu and J. Zhang, *Adv. Mater.*, 2024, **36**, 2313749.
- 20 X. Liu, C. Liu, J. Zhou, X. Zhao, Y. Shen, H. Cong and B. Yu, *Talanta*, 2024, **273**, 125830.
- 21 D. R. Hirmas, D. Gimenez, A. Nemes, R. Kerry, N. A. Brunzell and C. J. Wilson, *Nature*, 2018, **561**, 100–103.
- 22 K. Kodama, M. Obata and T. Hirose, *ChemPlusChem*, 2024, **89**, 2400021.
- 23 L. Chang, Q. Li, P. Weidler, Z. Gu, C. Woll and J. Zhang, *CCS Chem.*, 2022, **4**, 3472–3481.
- 24 X. X. Yang, N. Li, C. Li, Z. B. Jin, Z. Z. Ma, Z. G. Gu and J. Zhang, *J. Am. Chem. Soc.*, 2024, **146**, 16213–16221.
- 25 T. Yang, S. Wang, H. Yang, H. Gui, Y. Du and F. Liang, *Adv. Funct. Mater.*, 2023, **33**, 2214183.
- 26 M. Wei, Y. Gao, X. Li and M. J. Serpe, *Polym. Chem.*, 2017, **8**, 127–143.
- 27 A. Iliopoulou, Z. Iatridi and C. Tsitsilianis, *Polymer*, 2024, **16**, 886.
- 28 A. Yamamoto, T. Inui, D. Suzuki and K. Urayama, *Soft Matter*, 2023, **19**, 9082–9091.
- 29 Y. Chen, T. Szkopek and M. Cerruti, *Mater. Horiz.*, 2023, **10**, 2638–2648.
- 30 W. Wang, Z. Liu, R. Wang, M. Cao, Y. Chen, X. Lu, H. Ma, T. Yue and T. Yan, *Chem. Eng. J.*, 2023, **470**, 143967.
- 31 J. Liu, L. Jiang, S. He, J. Zhang and W. Shao, *Chem. Eng. J.*, 2022, **433**, 133496.
- 32 J. Tian, M. Pan, Y. Ma and J. W. Chew, *J. Membr. Sci.*, 2020, **593**, 117352.
- 33 C. Meng, Y. Sheng, Q. Chen, H. Tan and H. Liu, *J. Membr. Sci.*, 2017, **526**, 25–31.
- 34 X. Han, G. He, Y. He, J. Zhang, X. Zheng, L. Li, C. Zhong, W. Hu, Y. Deng and T. Y. Ma, *Adv. Energy Mater.*, 2019, **11**, 4915–4921.
- 35 M. Ali, S. Nasir and W. Ensinger, *Electrochim. Acta*, 2016, **215**, 231–237.
- 36 H. Xu, J. Wu, J. Liu, Y. Chen and X. Fan, *J. Mater. Sci.*, 2018, **29**, 17234–17244.
- 37 Y. Lin, F. Yu, Z. Yu, X. Lin, F. Lin, R. Liu, Q. Chen, J. Du, X. Huang, A. Gu, X. Li, S. Arcadio, S. Fang, W. Ye and J. Lin, *Sep. Purif. Technol.*, 2024, **341**, 126919.
- 38 Y. Chen, L. Xia and G. Li, *J. Chromatogr. A*, 2022, **1677**, 463341.
- 39 N. Gowriboy, R. Kalaivizhi, N. J. Kaleekkal, M. R. Ganesh and K. A. Aswathy, *J. Environ. Chem. Eng.*, 2022, **10**, 108668.
- 40 S. Fang, P. Zhang, J. Gong, L. Tang, G. Zeng, B. Song, W. Cao, J. Li and J. Ye, *Chem. Eng. J.*, 2020, **385**, 123400.
- 41 W. Li, Y. Li, X. Wen, Y. Teng, J. Wang, T. Yang, X. Li, L. Li and C. Wang, *J. Membr. Sci.*, 2022, **648**, 120369.
- 42 M. Pan, X. Zhang, J. Li, J. W. Chew and B. Pan, *ACS ES&T Water*, 2023, **3**, 1963–1971.
- 43 L. Solite and B. Seville, *Chirality*, 1997, **9**, 373–379.
- 44 C. Liu, R. Liang, X. Wang, J. Wang and J. Qiu, *J. Chromatogr. A*, 2013, **1294**, 145–151.
- 45 M. Gogoi, R. Goswami, A. Borah and S. Hazarika, *Sep. Purif. Technol.*, 2022, **283**, 120201.
- 46 X. Li, X. Li, T. Xia, W. Chen, K. J. Shea and X. Lu, *Mater. Horiz.*, 2023, **10**, 4452–4462.
- 47 J. Fan, J. Lai, C. Huang, Z. Lai, C. Xie, H. Chen, H. Peng and Y. Liu, *Sep. Purif. Technol.*, 2024, **328**, 124999.
- 48 G. N. Roviello, G. Oliviero, A. Di Napoli, N. Borbone and G. Piccialli, *Arab. J. Chem.*, 2020, **13**, 1966–1974.
- 49 G. Zhao and W. Chen, *Appl. Surf. Sci.*, 2017, **398**, 103–115.
- 50 M. Gogoi, R. Goswami, A. Borah, H. Sarmah, P. Rajguru and S. Hazarika, *Sep. Purif. Technol.*, 2021, **279**, 119704.
- 51 H. Li, J. Liao, T. Xiang, R. Wang, D. Wang, S. Sun and C. Zhao, *Desalination*, 2013, **309**, 1–10.
- 52 Z. Zandi, M. Rastgar, M. Mohseni, M. D. Firouzjaei, W. Diloekunakul, B. Anasori, C. D. Vecitis, R. Keller, M. Wessling, M. Elliott, A. Rahimpour and M. Sadrzadeh, *Adv. Funct. Mater.*, 2024, **34**, 2401970.
- 53 S. Minic, B. Annighofer, A. Helary, D. Hamdane, G. Hui Bon Hoa, C. Loupiac, A. Brulet and S. Combet, *Biophys. J.*, 2020, **119**, 2262–2274.
- 54 Y. Ma, X. Cheng, H. Ma, Z. He, Z. Zhang and W. Zhang, *Chem. Sci.*, 2022, **13**, 13623–13630.
- 55 A. Baral, L. Satish, D. P. Das, H. Sahoo and M. K. Ghosh, *New J. Chem.*, 2017, **41**, 8130–8139.